Essential Chem

ISSN: 2837-8083 (Online) Journal homepage: www.tandfonline.com/journals/tess20

A versatile and practical synthesis of oxygen evolution catalysts

Christian L. Conrad, Welman Curi Elias, Hunter P. Jacobs, Austin M.K. Fehr , Sadegh Yazdi, Tanguy Terlier, Aditya D. Mohite & Michael S. Wong

To cite this article: Christian L. Conrad, Welman Curi Elias, Hunter P. Jacobs, Austin M.K. Fehr , Sadegh Yazdi, Tanguy Terlier, Aditya D. Mohite & Michael S. Wong (2025) A versatile and practical synthesis of oxygen evolution catalysts, Essential Chem, 2:1, 2489957, DOI: 10.1080/28378083.2025.2489957

To link to this article: https://doi.org/10.1080/28378083.2025.2489957

© 2025 The Author(s). Published with license by Taylor & Francis Group, LLC.

View supplementary material

Published online: 28 Apr 2025.

Submit your article to this journal

Article views: 292

View related articles

View Crossmark data

Full Terms & Conditions of access and use can be found at https://www.tandfonline.com/action/journalInformation?journalCode=tess20

ESSENTIAL CHEM
2025, VOL. 2, NO. 1, 1–13
https://doi.org/10.1080/28378083.2025.2489957

Taylor & Francis
Taylor & Francis Group

OPEN ACCESS Check for updates

A versatile and practical synthesis of oxygen evolution catalysts

Christian L. Conrad[a], Welman Curi Elias[a], Hunter P. Jacobs[a*], Austin M.K. Fehr[a], Sadegh Yazdi[b], Tanguy Terlier[c], Aditya D. Mohite[a,d], and Michael S. Wong[a,d]

[a]Department of Chemical and Biomolecular Engineering, Rice University, Houston, TX, USA; [b]Renewable and Sustainable Energy Institute, University of Colorado, Boulder, CO, USA; [c]SIMS Laboratory, Shared Equipment Authority, Rice University, Houston, TS, USA; [d]Rice Advanced Materials Institute, Rice University, Houston, TX, USA

ABSTRACT
State-of-the-art OER (oxygen evolution reaction) catalyst syntheses require the use of expensive metals (*i.e.* Ir) with complex and time-consuming synthetic routes, difficulty in control, and impractical yields. Although some reported catalysts show improved performance (*i.e.* activity, stability, lowering Ir content with Ru), their synthesis is costly and not viable for scale-up. Here we demonstrate a practical, reliable, and scalable one-pot synthesis method for OER catalysts based on borohydride reduction to quickly yield >100 mg of Ir, Ru, and IrRu nanoparticles (1.6 ± 0.2 nm) with outstanding batch-to-batch consistency. Both mono- and bi-metallic compositions exhibit a metal-core/metal-oxide-shell nanoparticle structure. We further demonstrate the versatility of this method by incorporating earth-abundant yttrium, resulting in a catalyst with improved precious metal utilization for OER. This method serves as a robust platform for generating ultrasmall (<2 nm) multi-metal particles useful for electrocatalysis research.

ARTICLE HISTORY
Received December 27, 2024
Accepted March 31, 2025

KEYWORDS
Alloys; electrocatalysts; iridium; nanoparticles; ruthenium

1. Introduction

Global hydrogen (H_2) demand has nearly tripled since 1980 (from ~25 to ~72 million metric tons in 2019)[1,2] and is projected to grow at an even greater rate over the next few decades as a result of rising decarbonization efforts.[3,4] However, >95% of all H_2 is currently sourced from hydrocarbon feedstocks, with steam methane reforming alone accounting for ~3% of all CO_2 emissions;[5] only ~4% of H_2 is derived from more carbon-neutral electrolysis processes.[6]

Mature alkaline water electrolyzers (AWE) use Earth-abundant catalysts, but the porous separator limits their achievable current densities and overall cell efficiency, resulting in limited market penetration. Zero-gap cells using polymer membrane electrolytes, however, show great promise. Small-scale (*i.e.*, 100-10,000 kg-H_2/d) systems have been deployed with alkaline (anion exchange membrane, AEMWE) or acidic (proton exchange membrane, PEMWE) media, although the latter shows greater promise achieving 3-4 × greater current densities due to inherently lower ohmic losses and more robust ionomer/membrane stabilities.[6–8]

Despite this potential, PEM H_2 struggles to be cost-competitive with established hydrocarbon-based technologies. At a rough average of US$4 per kg H_2 (with a wide range of ~$3-12/kg-$H_2$),[9,10] PEM H_2 remains at least 4× more expensive than the U.S. Department of Energy's recent "111" goal to achieve $1/kg-$H_2$ in one decade (*ca.* 2030).[11] While reductions in operating expenses are expected to arise from an increasing availability of low-cost renewable energy sources, material costs for the catalyst/membrane assemblies still represent the majority of the initial investment for PEM stacks.[6,12,13] Commercial PEM electrolyzers consist of a Pt/C cathode to drive the hydrogen evolution reaction (HER) and an IrO_x anode to catalyze the corresponding oxygen evolution reaction (OER); although these rare-earth elements are expensive (i.e., ~$4,725 and ~$950 USD oz-1 for Ir and Pt, respectively as of July 2024), the more pressing concern for global deployment is their sheer scarcity.

Modern small-scale PEM electrolyzers (i.e., 50-200 kW) can operate at ~2 A cm^{-2} for 5-10 year lifetimes[8,13,14] with catalyst loadings of 0.5–1.0 mg-Pt and 2.0-2.5 mg-IrO_x per cm^2.[15] As PEM capacity moves past the GW scale however, these loadings will be unsustainable;[16,17] Ir in particular presents an immediate bottleneck and will need to be reduced by at least an order of magnitude (e.g., 0.05–0.1 mg-IrO_x cm^{-2}) to feasibly meet H_2 demand.[13,17] Even alloying Ir with other costly and scarce

CONTACT Aditya D. Mohite mswong@rice.edu Department of Chemical and Biomolecular Engineering, Rice University, Houston, TX 77005, USA
*Present address: Manufacturing Science Division, Oak Ridge National Laboratory, 1 Bethel Valley Road, Oak Ridge, TN 37830, USA

Supplemental data for this article can be accessed online at https://doi.org/10.1080/28378083.2025.2489957

© 2025 The Author(s). Published with license by Taylor & Francis Group, LLC.
This is an Open Access article distributed under the terms of the Creative Commons Attribution License (http://creativecommons.org/licenses/by/4.0/), which permits unrestricted use, distribution, and reproduction in any medium, provided the original work is properly cited. The terms on which this article has been published allow the posting of the Accepted Manuscript in a repository by the author(s) or with their consent.

elements, such as Ru, can be a viable approach to reaching this target from the perspective of global resource management.16 Reducing electrolyzer precious metal loading remains a highly active research area even with "benchmark" commercial catalysts. Beyond high intrinsic activity and stability, additional catalyst design considerations that impact electrolyzer performance includes catalyst packing density (*i.e.*, mgcat cm^{-3}), layer uniformity, intrinsic catalyst conductivity, membrane thickness, and stack architecture.[18–20]

As the societal importance of OER research grows,[21] the state-of-the-art methods for synthesizing Ir-based catalysts, including the molten salt method,[22,23] pulsed laser ablation,[24,25] wet chemistry,[26,27] and solution combustion synthesis,[28] often require highly specific conditions, such as an anhydrous environment, high operating temperatures, specialized metal precursors, limited morphology control, and challenging scalability.It is our opinion that there is a need for a widely accessible, robust, and highly reproducible method of synthesizing OER catalysts. Here, we report the development of a new method to prepare OER catalysts with different metal compositions without the requirement of an anhydrous environment which allowed the utilization of a large number of shelf-stable precursors, improved reproducibility, and resulted in excellent catalyst yield. Our goal with this work is to provide a tool that can help bridge the gap between state-of-the-art catalyst design and fundamental PEM research.

2. Materials and methods

2.1. Materials

Iridium (III) chloride hydrate ($IrCl_3$ xH_2O) [99.9% Trace Metals Basis], ruthenium (III) chloride hydrate ($RuCl_3$ xH_2O) [99.98% Trace Metals Basis], yttrium (III) chloride hexahydrate (YCl_3 $6H_2O$) [99.9% Trace Metals Basis], hexadecyltrimethylammonium bromide (CTAB | $CH_3(CH_2)_{15}N(Br)(CH_3)_3$) [BioXtra, ≥99%], sodium borohydride ($NaBH_4$) [*ReagentPlus®*, 99%], 2-propanol [IPA, anhydrous, 99.5%], perchloric acid ($HClO_4$) [ACS Reagent, 70%], and Nafion™ 117 solution [~5% in lower aliphatic alcohols and water] were all purchased from Sigma-Aldrich and used without further treatment or purification. Sulfuric acid (H_2SO_4) [72 w/w %, 24.0 ± 0.1 N, 12 M] was purchased from LabChem™, Vulcan XC 72 R (*i.e.*, Carbon Black) [ρ_{Bulk} ~ 96 kg m^{-3}, d ~ 50 nm] from the Fuel Cell Store, ethanol (EtOH | CH_3CH_2OH) [200 proof, USP] from Decon™ Labs, graphite rods (0.615 cm diameter × 15.2 cm long, 99.9995% metal basis, SPK grade, Ultra "F" 500 purity) from Alfa Aesar, and all water (H_2O | DI) was generated on-site using a Millipore Direct-Q3 system [18.2 MΩ at 25 °C]. Nitrogen (N_2) [High Purity Grade], oxygen (O_2) [Ultra High Purity Grade], and argon (Ar) [Ultra High Purity Grade] gases were all purchased from AirGas.

$NaBH_4$ was stored under vacuum desiccation to avoid degradation. Glassware was cleaned between each use beginning with rinsing and sonicating in water, followed by at least a three-hour soak in freshly prepared Aqua Regia to dissolve residual precious metals before finally being rinsed thoroughly in DI water and oven dried. Note that separate stir bars were used for each catalyst composition but reused (after cleaning) for each of the three batches.[1]

2.2. Catalyst synthesis

In a typical experiment, 1 mmol of metal chloride hydrate salt was dissolved in 50 mL of the mixed EtOH-H_2O solvent. Meanwhile, in a jacket reactor vessel 450 mL of the same mixed solvent was used to dissolve 10 mmol of CTAB as the contents were cooled to 15 °C. Once the target temperature was reached, the salt mixture was added to a pressure-equalizing dropping funnel affixed to the top of the jacketed reactor, and a glass-frit sparger was submerged into the funnel. Nitrogen gas (N_2) was bubbled through the salt mixture which then flowed through the pressure-equilibration tube to blanket the CTAB solution below. Quickly, 20 mmol of $NaBH_4$ powder was charged to the CTAB solution and allowed to dissolve completely (~10 mins) under vigorous mixing; immediately prior to this step, constant pH sampling of the reactor began.

Once the partial solvolysis of $NaBH_4$ had increased the pH of the CTAB/$NaBH_4$ solution to ~11.5 ± 0.2 (Figure 1(b)), the funnel was opened, and the salt solution was rapidly (<90s) introduced. Immediate gas evolution accompanied by a change in the solution color was observed (Figures S1–S4). This reactor content was allowed to equilibrate overnight (*i.e*, 15.5 – 16 hrs) under constant stirring and N_2 flow. Particles were recovered through repeated centrifugation and washing with fresh EtOH-H_2O solvent before drying for 12 ± 0.5 hrs in a vacuum oven (65°C, −25 psig). Full experimental details are provided in the SI. All syntheses were performed in triplicate, and particle characterization was performed for each batch individually to report, where appropriate, the average. The temporal changes in pH and temperature within the reactor media were monitored and recorded using the Thermo Scientific Orion Star Com software, connected to a Thermo Scientific Orion STARA2115 pH and temperature meter.

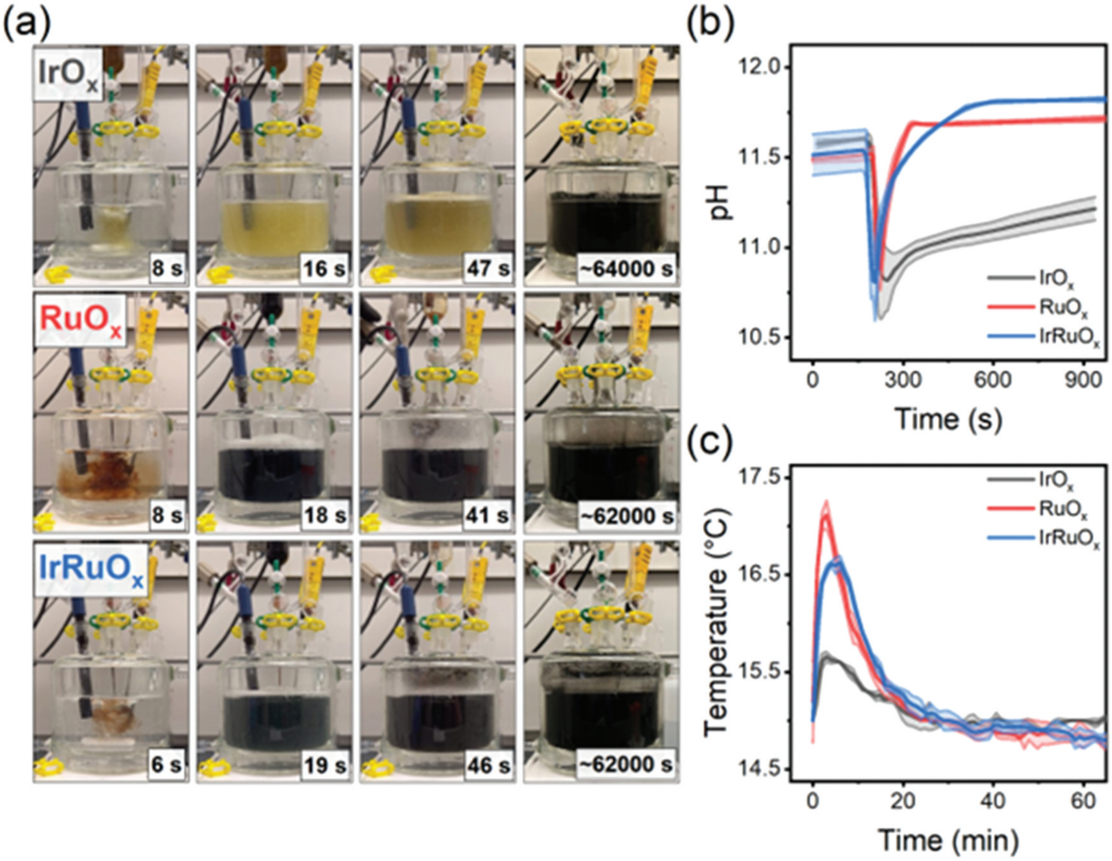

Figure 1. (a) Stills from the formation of (from top to bottom) Ir, Ru, and IrRu particles; t0 is taken to be the moment the metal-salt precursor solution is first introduced to the CTAB-$NaBH_4$ mixture below. (b) pH change of the main reactor contents as a function of time for the first ~15 mins. (c) Change in temperature of the main reactor vessel as a function of time for the first ~hour.

2.3. *Ink preparation*

The catalyst-to-carbon mass ratio was set to 2, the Nafion-to-solids (*i.e.*, catalyst plus carbon) ratio to 0.005%, the total 2-propanol-to-water mass ratio to 3, and the total weight loading of the ink to 0.3 wt.%. For simplicity, the ~50 wt.% lower aliphatic alcohols reported in the 5% Nafion stock solution have been treated as 2-propanol. Calculations were performed under the assumption that the density of the 5% Nafion solution, DI water, and 2-propanol were 0.924, 0.997, and 0.785 g mL^{-1}, respectively. Note also that Nafion was added to the final inks from a ~0.005 wt.% Nafion solution diluted with a 2-propanol-H_2O mixture.

2.4. *Scanning transmission electron microscopy*

High angle annular dark field scanning transmission electron microscopy (HAADF-STEM) images and energy-dispersive X-ray spectroscopy (EDS) maps were obtained using a probe Cs-corrected Thermo Scientific Titan Themis S/TEM equipped with a Super-X detector (four silicon drift detectors) operated at 80 kV. Catalyst particles were suspended in IPA that was then drop casted onto an ultrathin carbon film on Cu support TEM grid. The average particle size and size distribution were determined using ImageJ software from the HAADF-STEM images of at least 100 particles captured from different locations on the grid.

2.5. *Brunauer-emmett-teller surface area*

BET surface area measurements were performed on an Autosorb-iQ-MP system measured at liquid-N_2 temperature (77 K). Prior to each measurement, samples were degassed for 12 hr under vacuum (~2 mmHg) at 80 °C.

2.6. *X-ray powder diffraction*

XRD was collected with a Philips X'Pert Pro equipped with a Cu Kα radiation source (1.540598 Å). Analysis was conducted in a 2θ range of 15-90°, with a step size of 0.0050 s^{-1}. Reference spectra were taken from the online database provided by The Materials Project.[2]

2.7. X-ray photoelectron spectroscopy

XPS was performed on a PHI Quantera SXM (ULVAC-PHI. Inc) spectrometer equipped with an Al monochromator. Samples were analyzed at the Ir 4 f, Ru 3d, and Y 3d core levels. The C 1s core level was also measured in order to normalize binding energy values to the adventitious carbon C 1s peak at 284.8 eV. Since the C 1s and Ru 3d regions overlap, the O 1s core level was alternatively used as a secondary reference for samples containing Ru. XPS peak fittings and surface metal compositions were calculated using Multipak (ULVAC-PHI. Inc) XPS fitting software.

2.8. Time-of-flight secondary ion mass spectrometry

Positive high mass resolution depth profiles were performed using a ToF-SIMS NCS instrument, which combines a ToF-SIMS instrument (ION-TOF GmbH, Münster, Germany) and an *in situ* Scanning Probe Microscope (NanoScan, Switzerland). The analysis field of view was 80 × 80 μm^2 (Bi^{3+} @ 30 keV, 0.35 pA) with a raster of 128 × 128 along with the depth profile. A charge compensation with an electron flood gun has been applied during the analysis. An adjustment of the charge effects has been operated using a surface potential of −36 V and an extraction bias of 0 V. The cycle times was fixed to 90 µs (corresponding to m/z = 0-735 amu mass range). The sputtering raster was 450 × 450 μm^2 (Cs^+ @ 1 keV, 44 nA). The beams were operated in non-interlaced mode, alternating 1 analysis cycle and 1 frame of sputtering (corresponding to 1.31 s) followed by a pause of 2 s for the charge compensation. The $MC_{s_n^+}$ (n = 1, 2) depth profiling has also been used to improve the understanding of the data.

This is a useful method, mainly applied to quantify the alloys but also to identify any ion compounds. The cesium primary beam is used for sputtering during the depth profile and permits the detection of MC_{s^+} or $MC_{s_2^+}$ cluster ions where M is the element of interest combined with one or two Cs atoms. The advantages of following MC_{s^+} and $MC_{s_2^+}$ ions during ToF-SIMS analysis include reducing matrix effects and the possibility of detecting the compounds from both electronegative and electropositive elements and compounds. All depth profiles have been point-to-point normalized by the total ion intensity.

2.9. Electrochemical activity

OER activity was assessed in 30 ± 1 mL of in O_2 – saturated 0.1 M $HClO_4$ using a Rotating Disk Electrode (RDE) equipped with a 5 mm diameter polished glassy carbon electrode tip at 1600 RPM. A graphite rod and double-junctioned Ag|AgCl (sat. KCl) electrode functioned as the counter and reference, respectively. The reference electrode was calibrated using Pt electrodes in H_2-saturated electrolyte weekly to ensure stability. The catalyst ink was drop-cast onto the glassy carbon tip in <5 µL increments (varied by exact ink loading) to a final loading of 100 $\mu g_{\mathrm{Catalyst}}$ $cm^{-2}{}_{\mathrm{Geo}}$. The electrochemical activity was normalized by precious metal content,[3]

$$j_{PM}(\eta) = \frac{i}{m_{\mathrm{Cat}} \cdot \%_{\mathrm{PM}}} \tag{1}$$

where j_{PM} is the precious metal based current density $\left(\mathrm{mA\ mg_{PM}^{-1}}\right)$, η is overpotential of the reaction at the measured conditions (mV), i is measured current (mA), m_{Cat} is the total mass of catalyst loaded/deposited on the electrode (mg), and $\%_{\mathrm{PM}}$ is the weight percent of the catalyst of Ir + Ru (%).

2.10. Miscellaneous equipment

Online temperature measurements during catalyst synthesis were acquired using a K-Type thermocouple (J-KEM Scientific, Model 210). A FiveEasy™ Plus pH Meter (Mettler Toledo™) was used to record pH; the three-point calibration was checked daily, and all automatic temperature corrections were confirmed using the separate thermocouple readings. The jacketed reactor was stirred with a Fisher Scientific IsoTemp Hot Stir Plate (Cat # 11-610-49SH; 60 – 1,200 RPM).

3. Results and discussion

Although colloidal Ir synthesis methods benefit from decades of development,[29] the approach conceived here (Figure 1(a)) was inspired by the work of Lettenmeier et al.[30,31] They report highly active (*i.e.*, >100 A g Ir^{-1} at 1.51 V *vs.* RHE on an RDE) core-shell Ir-IrO_x nanoparticles after reducing dilute, anhydrous $IrCl_3$ (~1-2 mm) in the presence of CTAB surfactant via the slow addition of concentrated $NaBH_4$. With this method, high-purity ethanol (EtOH) significantly improved catalyst activity with ~100 and 10 fold-times as compared to H_2O or even low-H_2O mixtures, respectively (*i.e.*, 91.5 – 99.8% EtOH).[31] However, the use of anhydrous reagents requires specific reaction setups (*e.g.*, glove box, Schlenk lines, etc) and/or pre-treating the reagents/solvents to remove any trace of water present.

We sought to circumvent the restrictions of an anhydrous environment in order to utilize a wider array of shelf-stable precursors (*e.g.*, metal hydrates, acetates), investigate the feasibility of mixed metal materials, and ease reproducibility through less restrictive conditions (See also The Role of CTAB in this Synthesis in SI). We hypothesized that the poor reported performance of the water-rich synthesis may be explained by the insolubility of anhydrous $IrCl_3$ in H_2O coupled with the competing hydrolysis of $NaBH_4$ during the slow introduction of the reductant – leading to a significantly lower concentration than the stoichiometric target. Our approach closely follows early reports on the synthesis of amorphous metal boride nanoparticles. The BH_4^- driven reduction of transition metals (*e.g.*, Co, Fe, Ni, Cu)[32–38] to form metallic and/or metal-boron mixed particles has been employed since the early 1950′s[39–41] and has subsequently been applied metal oxides[42,43] as well as noble metals.[44–46] The nature of the salt, solvent, temperature, dissolved oxygen, pH, mixing speed/order, and more can all heavily impact the kinetics and product distribution (*i.e.*, M, M_xB, M-B, etc.) of these reactions.[40,47] Perhaps the most significant shortcoming of this approach is the poor control over particle size. Although a given condition typically produces a monodisperse suspension, fine-tuning the particle size *a priori* is not trivial.

Under aqueous conditions, rapid mixing of the metal and reductant can lead to smaller particle size, presumably due to more rapid nucleation,[34,36] but this appears dependent on the metal identity. Alternatively, solvent changes appear to provide a more consistent and predictable means of manipulating particle size. Although examples are limited, performing the reduction step in polar, protic linear alcohols (*i.e.*, methanol through butanol) appears to impart slower reaction kinetics and smaller particle sizes compared to the aqueous systems.[38] It is postulated that some combination of the solvent's dielectric constants and viscosity are primarily responsible for the empirical observations, but no predictive model has been proposed. Notably, even early reports for mixed solvents (*i.e.*, water/ethanol) describe reduced particle size, although no detailed explanation is provided.[37]

Similarly, surfactant-assisted approaches (in both aqueous[48] and mixed[49,50] solvents) provide smaller average particle sizes with narrower size distributions as compared to the surfactant-free systems without influencing the composition. Once again, however, the exact mechanism by which these surfactants operate is ambiguous. Taking CTAB as an example, not only is solvent viscosity and interfacial tension influenced, but the formation of micelles with a positive surface charge may serve to "scavenge" counterions and concentrate the target metal cations in the interstitial solvent between the close-packed micelles.[49,50] It should be emphasized that while this latter mechanism is plausible, direct evidence is severely lacking.

As a result, we chose to use more soluble metal hydrates (*e.g.*, $IrCl_3{\cdot}xH_2O$) and implement a mixed EtOH-H_2O solvent [χ_{EtOH} ~ 30]. Associated with the use of more soluble metal hydrates which will facilitate the preparation of the catalysts, we also designed a bimetallic $IrRuO_x$ catalyst, aiming to reduce the usage of Ir and therefore its material cost. As a control, monometallic IrO_x, and RuO_x were also prepared.

As illustrated in Figure 1(b,c), respectively, the degree/rate of both pH and temperature changes are more rapid as the Ru concentration increases from Ir to IrRu to Ru – a trend which is further reflected in the Y-diluted particles to be discussed later (Figures S5 and S6). Qualitatively, this observed reaction rate is also seen in the degree of (presumably H_2) gas formation indicated by the CTAB foaming in the reactor headspace. We note, however, that these observations do not necessarily imply a more rapid reduction of the Ru species as compared to other metals. Metallic Ru (Ru^0) is known to be an effective catalyst for exothermic borohydride solvolysis reactions,[25] and some portion of this initial reactivity can likely be attributed to these competing processes. In fact, accounting for this loss of reductant motivated the choice for a great excess (20× salt mass) of $NaBH_4$ used here (See also, *Comments on $NaBH_4$ Excess* inSI).

Physically, the recovered materials all take the form of distinct spherical particles (<3 nm) agglomerated into clusters or "chain networks," similar to previous reports.[31,51,52] HAADF-STEM imaging (Figure 2) reveals that the particles are remarkably uniform and exhibit a tight size distribution of 1.4 ± 0.4, 1.8 ± 0.5, and 1.8 ± 0.6 nm (diameter) for Ir, Ru, and IrRu, respectively. This small particle size is further reflected in the BET surface area measurements of 29.1 ± 1.2, 1.6 ± 0.6, and 33.5 ± 2.1 $m^2\ g^{-1}$, for Ir, Ru, and IrRu, respectively (Figure S7). As expected for particles of this size, XRD analysis provides little definitive insight into the structural nature of these materials. Very broad peaks indicative of metallic Ir (ca. 40°, 69°, 83°) and Ru (ca. 44°) can be observed in both the mono- and bi-metallic particles, and the spectra appear nearly identical between batches (Figure S8, Table S2).

Fortunately, XPS provides compelling evidence of the mixed structure of these particles. As illustrated in Figures 3(a,d) and S13 the monometallic IrO_x particles exhibit a near-equal quantity of metallic (Ir^0) and oxidized (IrO_2) iridium,[53] comparable to previous reports of ~85/15 at.% Ir^0/ IrO.[30] Conversely, the pure Ru particle does not show metallic character and instead

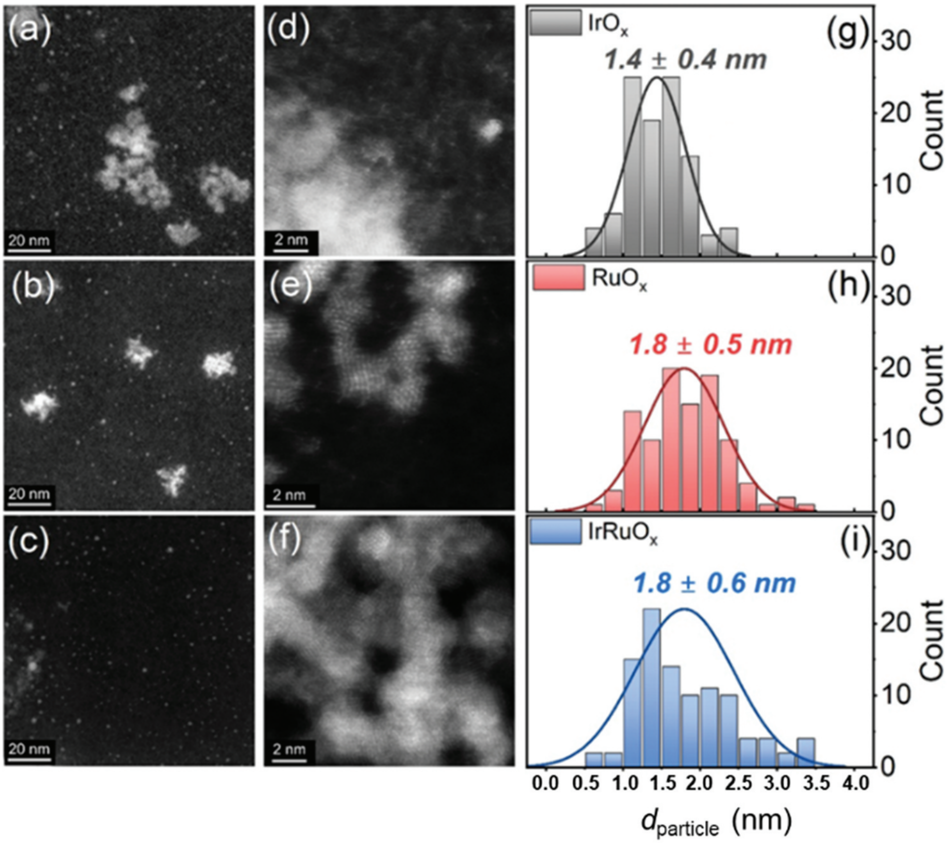

Figure 2. Representative HAADF-STEM images of (a,d) IrO$_x$, (b,e) RuO$_x$, and (c,f) IrRuO$_x$ particles. The corresponding histograms of 100 measured particles are presented in Panels g, h, and i, respectively.

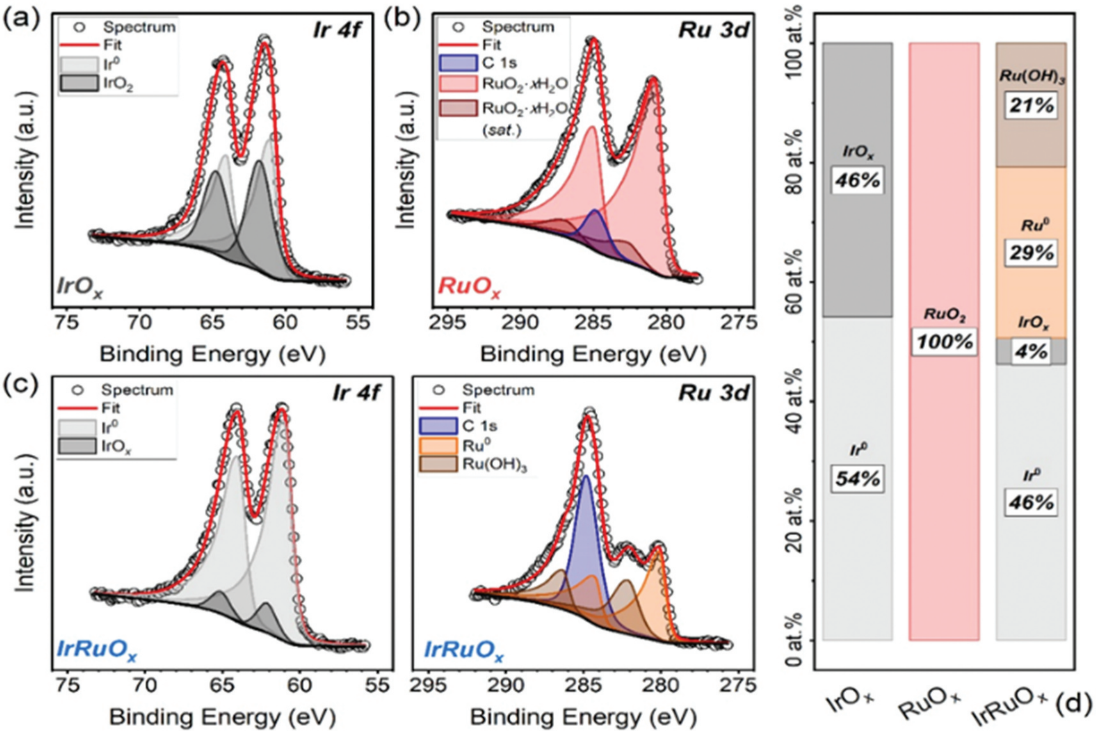

Figure 3. XPS spectra of Ir 4 f for both the IrO$_x$ (a) and IrRuO$_x$ (c, left) particles are presented alongside the Ru 3d spectra of RuO$_x$ (b) and IrRuO$_x$ (c, right). The total atomic composition is summarized in panel (d).

reveals a hydrated oxide, as supported by the shape of the O 1s peak, with trace evidence of carbon contamination, presumably due to residual CTAB.[54] (Figures 3(b,d) and S14) Specifically, although the Ru 3d and C 1s regions overlap, the C 1s peak location is characteristic of C-C and C-H bonds. This surprising evidence of a persistent hydrous oxide, despite all samples undergoing prolonged drying in a vacuum oven, helps reconcile the lower BET surface area of RuO_x compared to the other samples. Despite a similar particle size, many of the potential N_2 adsorption sites are occupied by the hydrous layer.

XPS of the bimetallic $IrRuO_x$ provides the most conclusive indication of alloying. (Figures 3(c) and S15) First evaluating iridium, metallic Ir^0 now dominates the Ir speciation (*i.e.*, ~90% of total Ir vs 50% in the monometallic), but maintains a similar total fraction of the composition. Moreover, the shifting of the IrO_x peak to a higher binding energy than the monometallic IrO_2 indicates a mixed oxide with multiple oxidation states.[55] The more striking consequence of alloying can be observed in the ruthenium signal in which ~60% of the species now portrays metallic character (Ru^0). The remaining ~40% is attributed to a Ru^{3+}-hydroxide species, rather than RuO_2, due to the shift in binding energy. In other words, the total metallic species (*i.e.*, Ir^0 + Ru^0) occupy ~75% of the particle compared to ~25% oxide/hydroxide. If the particle is to fit our proposed oxide shell over metal core model, these XPS data suggest that the metallic core may be slightly Ir-rich, while the shell is slightly Ru-rich. This model is partially supported by EDS mapping at 80 kV (Figure S10).

Although these XPS results can be fitted to our core-shell model, we sought to corroborate this hypothesis utilizing ToF-SIMS depth profiling. It should be noted that although ToF-SIMS lacks the lateral resolution to isolate a single particle, the signal received from sputtering still provides insight into the average aggregate composition with nm-scale sensitivity. Profiling of the IrO_x particles shows clear evidence of the metallic species (*e.g.*, Ir+) increasing in intensity in proportion to a decrease in intensity from the higher oxide species (*e.g.*, IrO_2+, $Ir_2O_3^+$). (Figures 4(a) and S21-22)

The opposite trend is observed with RuO_x: the Ru^+ ion signal rapidly decreases, while the RuO_2^+ ion signal increases and stabilizes after a few seconds of sputtering. This behavior suggests that the RuO_x nanoparticles exhibit a homogeneous ruthenium oxide composition from the surface to the core. The exception is the first

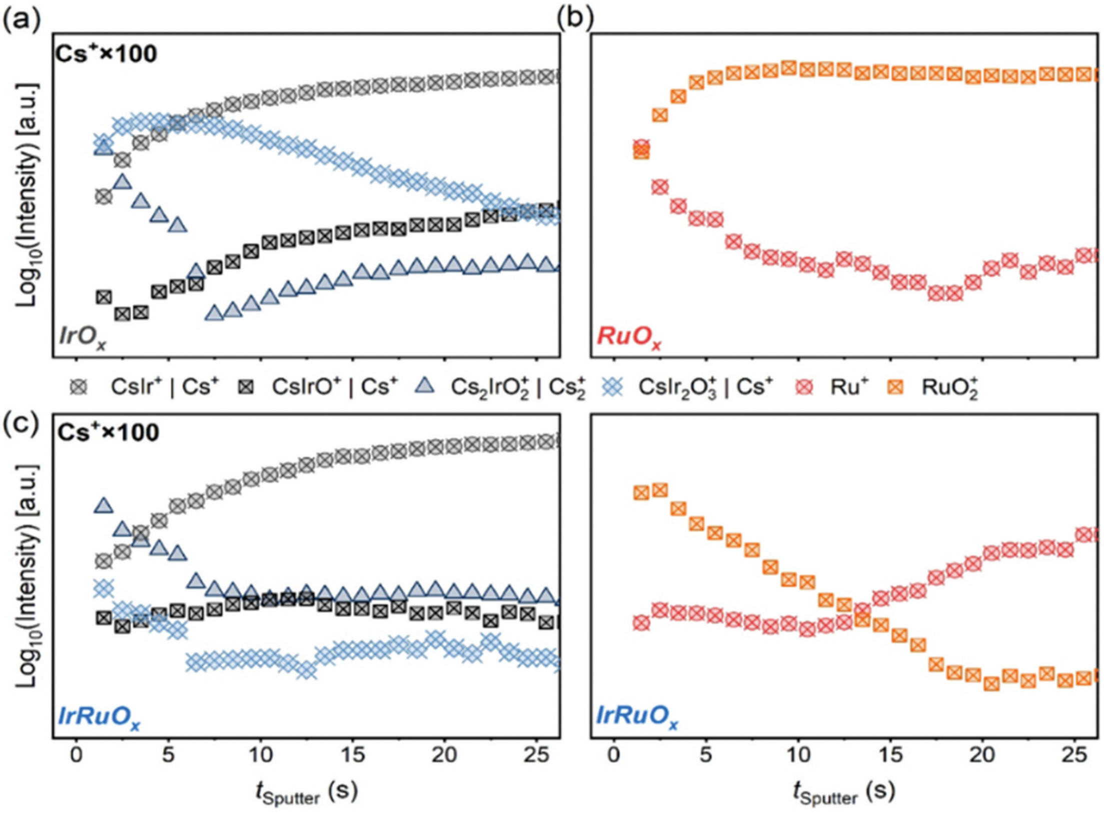

Figure 4. ToF-SIMS results is presented for the first 25 seconds of sputtering for (a) IrO_x, (b) RuO_x, and (c) $IrRuO_x$. Note that the species normalized by Cs^+ have been amplified by 10× for this illustration.

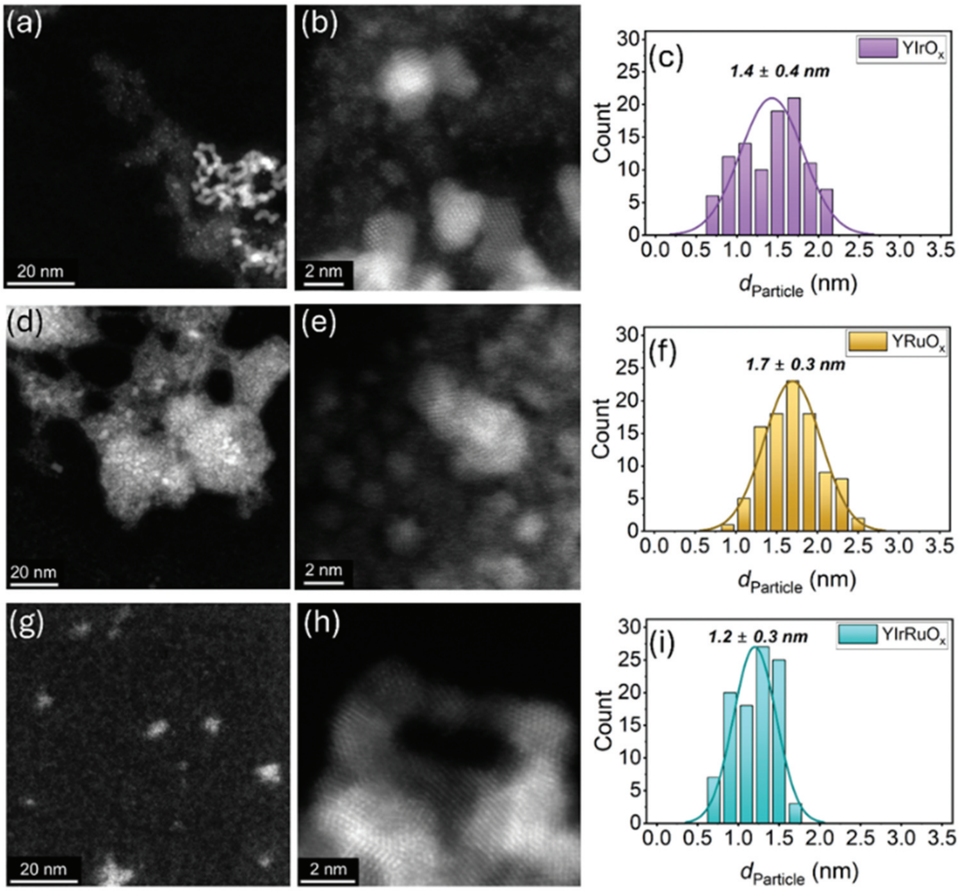

Figure 5. Representative HAADF-STEM images of (a,b) YirO$_x$, (d,e) YruO$_x$, and (g,h) YirRuO$_x$ particles. An overlayed histogram of 100 measured particles is presented in Panel c,f and e respectively.

monolayer, which may be influenced by transient effects, surface contamination, or reactivity. This finding strengthens the argument that little to no metallic Ru is present in the monometallic particles. (Figures 4(b) and S23-24). In the bimetallic IrRuO$_x$, however, RuO$_2^+$ displays a pronounced dependence on particle depth, accompanied by a slight increase in metallic Ru species (*e.g.*, Ru$^+$) toward the particle core. The iridium speciation mirrors the monometallic case, with the exception that the IrO$^+$ species appears to diminish more rapidly in the alloyed core. (Figures 4(c) and S25-26)

With characterization of our Ir/Ru OER catalysts established, we were motivated to test the versatility of the synthesis method by incorporating a yttrium salt precursor. Here, we selected yttrium as the model due to its growing prevalence in the field.[56–58] We hypothesized that the rare-earth elements in these particles would have dispersed more finely, leading to greater accessibility for OER catalysis. Thus, four additional particles were synthesized: YO$_x$, YIrO$_x$, YRuO$_x$, and YIrRuO$_x$ in which the yttrium content was targeted at 50 at.% for the thrifted particles (synthesis images found in Figures S2 – S4).

Broadly, the Y/Ir/Ru particles exhibit comparable characteristics to the yttrium-free cases. Observations regarding the pH and temperature change align with the aforementioned trends (*i.e.*, Ru content corresponding to reaction rate), and the XRD spectra similarly provide little insight as yttrium lacks distinctive peaks between 2θ 30-90° in addition to obscuring the few notable peaks visible in the monometallic species (Figure S8). Notably, although the BET surface area of pure yttrium particles is significantly larger at 130 ± 1 m^2 g^{-1}, the surface area of YIrO$_x$, YRuO$_x$, and YIrRuO$_x$ are 22.6 ± 0.8, 31.0 ± 1.0, and 28.1 ± 0.2 m^2 g^{-1}, respectively – in line with IrO$_x$ and IrRuO$_x$ (Figure S7). As marked in Figure S9, the higher BET surface area of YO$_x$ is likely a result of the unreduced Y-Cl-O aggregates that can be seen under HAADF-STEM. Evidently, an additional metal is necessary to induce complete reduction of the yttrium chloride salt. However, this observation also provides the first indication that strong interactions between the precious metals and the Y oxides may be present in these materials, as opposed to being a simple mixture of particles.

As evident in Figure 5, the particles maintain the sub-3 nm dimensions at 1.4 ± 0.4, 1.8 ± 5, and 1.2 ± 0.3 nm

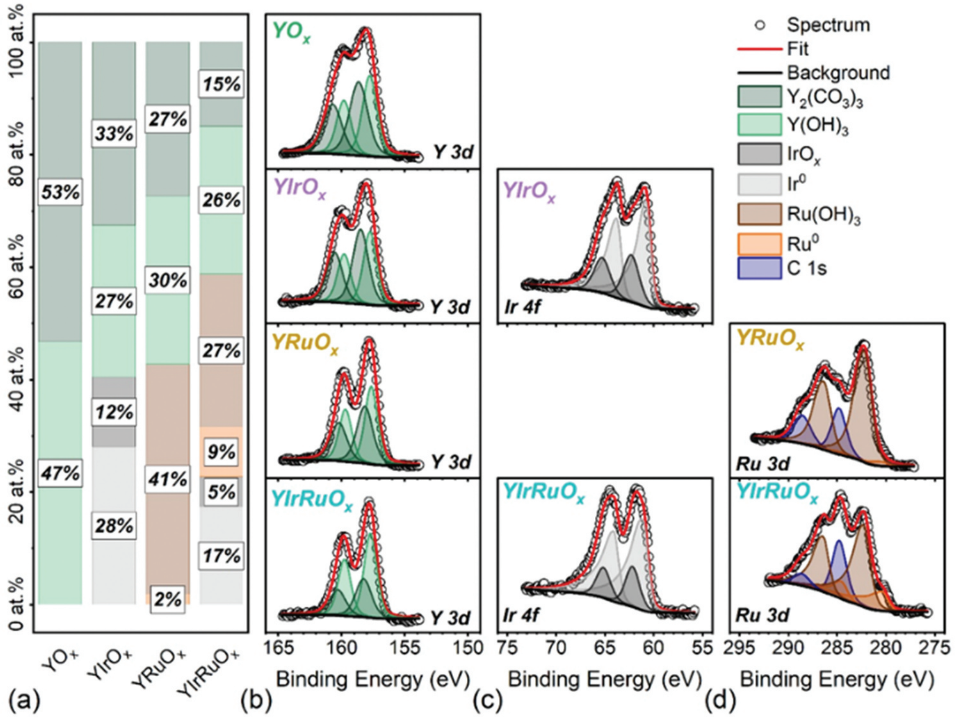

Figure 6. XPS spectra of (b) Y 3d for (from top to bottom) YOx, YIrO$_x$, YRuO$_x$, and YIrRuO$_x$ particles. (c) Ir 4 f of YIrOx (top) and YIrRuO$_x$ (bottom), and (d) Ru 3d of YRuO$_x$ (top) and YIrRuO$_x$ (bottom).

(diameter) for YIrO$_x$, YruO$_x$, and YirRuO$_x$, respectively. EDS mapping of YirO$_x$ (Figure S11), YruO$_x$ (Figure S12) underscore this structure and confirm that the “bright” particles observed in the HAADF-STEM images correspond to the precious metal species.

The speciation of yttrium appears roughly constant regardless of the precious metal species used. By XPS analysis, roughly half of the yttrium is present as hydroxide species[59] whilst the other half can most accurately be assigned to yttrium carbonate ($Y_2(CO_3)_3$)[60] (Figures 6(a,b) and S16-S19). We note that the Y 3d positions for Y_2O_3 and $Y(OH)_3$ can be similar, however, the O 1s region here is characteristic of Y-OH bonds rather than Y-O (which would appear <530 eV).[33] Therefore, this species is more likely the hydroxide form of Y^{3+}. Similarly, the presence of carbonate is also evident by C 1s peak around 289 eV. Although evidence of this carbonate species is unexpected, this is likely a result of ambient CO_2 reacting with the outermost Y_2O_3 surface once the particles are exposed to air after drying. This theory is supported by TOF-SIMS of the yttrium samples (Figure S29) which clearly show a strong signal of $Cs_2Y_2O_3^+$ on the outermost surface which diminishes rapidly to be replaced by lower oxides (*i.e.*, Y^+, YO^+, and $Y_2O_7^+$) when the sputtering depth increases.

Interestingly, the character of the precious metals more closely resembles the bimetallic IrRuO$_x$ case when thrifted with yttrium than their respective monometallic particles. In both YIrO$_x$ and YIrRuO$_x$, the Ir 4 f (Figure 6(c)) spectra mark the presence of both Ir0 and mixed IrO$_x$. Once again, ToF-SIMS confirms an increasing intensity of Ir+ moving toward the particle core, corresponding to a decrease in higher oxide signal. More notably, most of the Ru0 character is highly suppressed in both YRuO$_x$ and YIrRuO$_x$ in addition to being shifted to slightly higher binding energy, indicating loss of electron density and/or slight oxidation (Figure 6(d)). Physically, we hypothesize that this is a result of the Ru atoms preferentially dispersing throughout the yttrium oxide lattice as opposed to alloying with the Ir^0 rich core (in the case of YIrRuO$_x$). This suggests that iridium must be present to preserve metallic ruthenium through this synthesis method.

As a final proof of concept, both IrRuO$_x$ and YIrRuO$_x$ were assessed for OER activity in O_2 – saturated 0.1 M $HClO_4$ via and RDE at 1600 RPM (full experimental details in SI). As illustrated in Figure 7, this synthesis method yielded reproducible (Figures S35 and S36), and highly active catalysts which display a remarkable ~200 A g^{-1}Ir+Ru at 1.55 V *vs.* RHE and >400 A g^{-1}Ir+Ru at 1.60 V with ~50 at.% less iridium than reported monometallic Ir particles and, in the case of YIrRuO$_x$, only 40 µg Ir cm^{-2} Geo. While this initial screening should not be interpreted as a prediction of final PEM

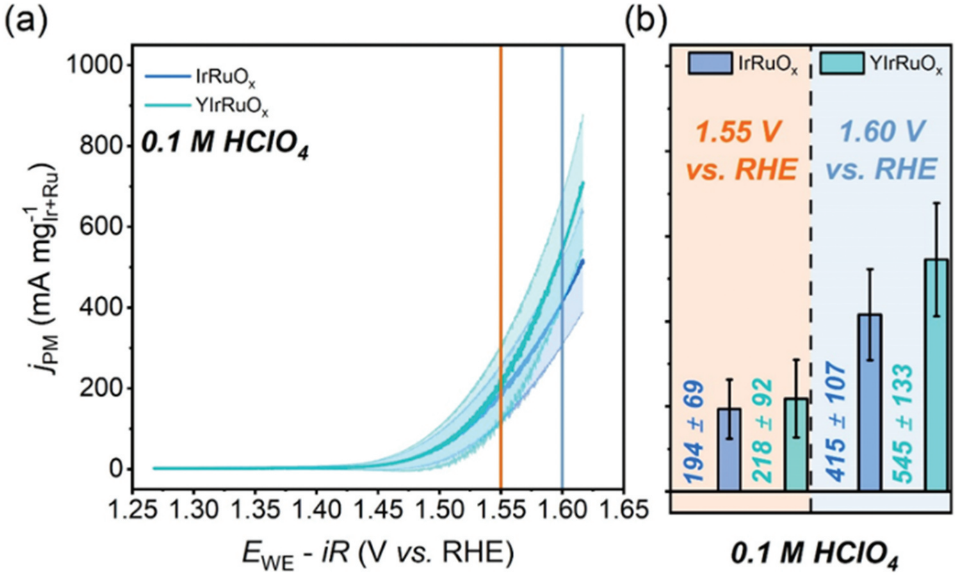

Figure 7. (a) OER current density normalized by total precious metal loading (Ir + Ru) of IrRuO$_x$ and YIrRuO$_x$ in 0.1 M HClO4 evaluated via RDE at 1600 RPM. (b) the corresponding precious metal activity at 1.55 (Orange) and 1.60 (blue) V *vs* RHE. Data presented as an average of six scans, for two trials of each of the three batches.

performance, it is an indication of the capacity of this protocol to synthesize highly active materials for the oxygen evolution reaction.

4. Conclusions

We report a robust, reproducible synthesis for mixed-metal nanoparticles with tunable composition and structure. This method requires no cost-prohibitive equipment, provides useful batch yields (*i.e.*, >100 mg) of <3 nm particles, and appears largely agnostic to the chosen metals (*i.e.*, other alloys of interest should be obtainable). We believe that the ease and versatility of this synthesis method holds promise for PEM development and electrocatalysis materials research.

Acknowledgments

A.D.M. and M.S.W. acknowledge the financial support provided by DE-EE0008843 through the HydroGEN Advanced Water Splitting Materials Consortium, part of the Energy Materials Network under the U.S. Department of Energy. The authors extend their appreciation to the Shared Equipment Authority at Rice University for training and the use of various instruments.

Author contributions

CRediT: **Christian L. Conrad:** Conceptualization, Data curation, Formal analysis, Investigation, Methodology, Writing – original draft, Writing – review & editing; **Welman Curi Elias:** Data curation, Formal analysis, Writing – review & editing; **Hunter P. Jacobs:** Formal analysis, Writing – review & editing; **Austin M.K. Fehr:** Data curation, Formal analysis, Writing – review & editing; **Sadegh Yazdi:** Data curation, Formal analysis, Investigation, Writing – review & editing; **Tanguy Terlier:** Data curation, Investigation, Writing – review & editing; **Aditya D. Mohite:** Conceptualization, Funding acquisition, Supervision, Writing – review & editing; **Michael S. Wong:** Conceptualization, Funding acquisition, Supervision, Writing – review & editing.

Disclosure statement

No potential conflict of interest was reported by the author(s).

Funding

This work was supported by the HydroGEN Advanced Water Splitting Materials Consortium [DE-EE0008843], part of the Energy Materials Network under the U.S. Department of Energy.

ORCID

Christian L. Conrad http://orcid.org/0000-0003-3048-6112
Welman Curi Elias http://orcid.org/0000-0002-9792-7392
Hunter P. Jacobs http://orcid.org/0000-0001-6190-874X
Sadegh Yazdi http://orcid.org/0000-0002-3470-9398
Tanguy Terlier http://orcid.org/0000-0002-4092-0771
Aditya D. Mohite http://orcid.org/0000-0001-8865-409X

References

[1] The Future of Hydrogen – Analysis. 2019. IEA [Internet]. https://www.iea.org/reports/the-future-of-hydrogen (accessed October 24, 2024).

[2] Hydrogen. IEA [Internet]. https://www.iea.org/energy-system/low-emission-fuels/hydrogen (accessed October 24, 2024).

[3] Energy Technology Perspectives 2020 – Analysis. 2020. IEA [Internet]. https://www.iea.org/reports/energy-technology-perspectives-2020 (accessed October 24, 2024).

[4] Net Zero by 2050 – Analysis. 2021. IEA [Internet]. https://www.iea.org/reports/net-zero-by-2050 (accessed October 24, 2024).

[5] Wismann, S. T.; Engbæk, J. S.; Vendelbo, S. B.; Bendixen, F. B.; Eriksen, W. L.; Aasberg-Petersen, K.; Frandsen, C.; Chorkendorff, I.; Mortensen, P. M. Electrified Methane Reforming: A Compact Approach to Greener Industrial Hydrogen Production. *Science*. 2019, *364*(6442), 756–759. DOI: 10.1126/science.aaw8775.

[6] Lagadec, M. F.; Grimaud, A. Water Electrolysers with Closed and Open Electrochemical Systems. *Nat. Mater.* 2020, *19*(11), 1140–1150. DOI: 10.1038/s41563-020-0788-3.

[7] Du, N.; Roy, C.; Peach, R.; Turnbull, M.; Thiele, S.; Bock, C. Anion-Exchange Membrane Water Electrolyzers. *Chem. Rev.* 2022, *122*(13), 11830–11895. DOI: 10.1021/acs.chemrev.1c00854.

[8] Ouimet, R. J.; Glenn, J. R.; De Porcellinis, D.; Motz, A. R.; Carmo, M.; Ayers, K. E. The Role of Electrocatalysts in the Development of Gigawatt-Scale PEM Electrolyzers. *ACS Catal.* 2022, *12*(10), 6159–6171. DOI: 10.1021/acscatal.2c00570.

[9] Glenk, G.; Reichelstein, S. Economics of Converting Renewable Power to Hydrogen. *Nat. Energy*. 2019, *4*(3), 216–222. DOI: 10.1038/s41560-019-0326-1.

[10] Guerra, O. J.; Eichman, J.; Kurtz, J.; Hodge, B.-M. Cost Competitiveness of Electrolytic Hydrogen. *Joule*. 2019, *3*(10), 2425–2443. DOI: 10.1016/j.joule.2019.07.006.

[11] Hydrogen Shot. Energy.gov [Internet]. https://www.energy.gov/eere/fuelcells/hydrogen-shot (accessed October 24, 2024).

[12] Mayyas, A.; Ruth, M.; Pivovar, B.; Bender, G.; Wipke, K. 2019. Manufacturing Cost Analysis for Proton Exchange Membrane Water Electrolyzers [Internet]. [place unknown]. (accessedOctober 24, 2024). DOI:10.2172/1557965.

[13] Ayers, K.; Danilovic, N.; Ouimet, R.; Carmo, M.; Pivovar, B.; Bornstein, M. Perspectives on Low-Temperature Electrolysis and Potential for Renewable Hydrogen at Scale. *Annu. Rev. Chem. Biomol. Eng.* 2019, *10*(1), 219–239. DOI:10.1146/annurev-chembioeng-060718-030241.

[14] Ayers, K. E.; Renner, J. N.; Danilovic, N.; Wang, J. X.; Zhang, Y.; Maric, R.; Yu, H. Pathways to ultra-low Platinum Group Metal Catalyst Loading in Proton Exchange Membrane Electrolyzers. *Catal. Today*. 2016, *262*, 121–132. DOI: 10.1016/j.cattod.2015.10.019.

[15] Kibsgaard, J.; Chorkendorff, I. Considerations for the Scaling-Up of Water Splitting Catalysts. *Nat. Energy*. 2019, *4*(6), 430–433. DOI: 10.1038/s41560-019-0407-1.

[16] Hubert, M. A.; King, L. A.; Jaramillo, T. F. Evaluating the Case for Reduced Precious Metal Catalysts in Proton Exchange Membrane Electrolyzers. *ACS Energy Lett.* 2022, *7*(1), 17–23. DOI: 10.1021/acsenergylett.1c01869.

[17] Minke, C.; Suermann, M.; Bensmann, B.; Hanke-Rauschenbach, R. Is Iridium Demand a Potential Bottleneck in the Realization of Large-Scale PEM Water Electrolysis? *Int. J. Hydrogen Energy*. 2021, *46*(46), 23581–23590. DOI: 10.1016/j.ijhydene.2021.04.174.

[18] Bernt, M.; Schramm, C.; Schröter, J.; Gebauer, C.; Byrknes, J.; Eickes, C.; Gasteiger, H. A. Effect of the IrO $_{x}$ Conductivity on the Anode Electrode/Porous Transport Layer Interfacial Resistance in PEM Water Electrolyzers. *J. Electrochem. Soc.* 2021, *168*(8), 084513. DOI: 10.1149/1945-7111/ac1eb4.

[19] Bernt, M.; Hartig-Weiß, A.; Tovini, M. F.; El-Sayed, H. A.; Schramm, C.; Schröter, J.; Gebauer, C.; Gasteiger, H. A. Current Challenges in Catalyst Development for PEM Water Electrolyzers. *Chem. Ing. Tech.* 2020, *92*(1–2), 31–39. DOI: 10.1002/cite.201900101.

[20] Kulkarni, D.; Huynh, A.; Satjaritanun, P.; O'Brien, M.; Shimpalee, S.; Parkinson, D.; Shevchenko, P.; DeCarlo, F.; Danilovic, N.; Ayers, K. E., et al. Elucidating Effects of Catalyst Loadings and Porous Transport Layer Morphologies on Operation of Proton Exchange Membrane Water Electrolyzers. *Appl. Catal. B Environ.* 2022, *308*, 121213. DOI: 10.1016/j.apcatb.2022.121213.

[21] Chen, F.-Y.; Wu, Z.-Y.; Adler, Z.; Wang, H. Stability Challenges of Electrocatalytic Oxygen Evolution Reaction: From Mechanistic Understanding to Reactor Design. *Joule*. 2021, *5*(7), 1704–1731. DOI: 10.1016/j.joule.2021.05.005.

[22] Ahmed, J.; Mao, Y. Ultrafine Iridium Oxide Nanorods Synthesized by Molten Salt Method toward Electrocatalytic Oxygen and Hydrogen Evolution Reactions. *Electrochim. Acta*. 2016, *212*, 686–693. DOI: 10.1016/j.electacta.2016.06.122.

[23] Lim, J.; Park, D.; Jeon, S. S.; Roh, C.; Choi, J.; Yoon, D.; Park, M.; Jung, H.; Lee, H. Ultrathin IrO$_2$ Nanoneedles for Electrochemical Water Oxidation. *Adv. Funct. Mat.* 2018, *28*(4), 1704796. DOI:10.1002/adfm.201704796.

[24] Zhong, W.; Lin, Z.; Feng, S.; Wang, D.; Shen, S.; Zhang, Q.; Gu, L.; Wang, Z.; Fang, B. Improved Oxygen Evolution Activity of IrO$_2$ by *in Situ* Engineering of an ultra-small Ir Sphere Shell Utilizing a Pulsed Laser. *Nanoscale*. 2019, *11*(10), 4407–4413. DOI: 10.1039/C8NR10163A.

[25] Wang, H.-B.; Wang, J.-Q.; Mintcheva, N.; Wang, M.; Li, S.; Mao, J.; Liu, H.; Dong, C.-K.; Kulinich, S. A.; Du, X.-W. Laser Synthesis of Iridium Nanospheres for Overall Water Splitting. *Materials*. 2019, *12*(18), 3028. DOI: 10.3390/ma12183028.

[26] Park, S.; Shviro, M.; Hartmann, H.; Mayer, J.; Carmo, M.; Stolten, D. Cation-Exchange Method Enables Uniform Iridium Oxide Nanospheres for Oxygen Evolution Reaction. *ACS Appl. Nano Mater.* 2022, *5*(3), 4062–4071. DOI: 10.1021/acsanm.2c00031.

[27] Xu, H.; Han, Y.; Wu, Q.; Jia, Y.; Li, Q.; Yan, X.; Yao, X. Iridium-Based Electrocatalysts for the Acidic Oxygen Evolution Reaction: Engineering Strategies

to Enhance the Activity and Stability. *Mater. Chem. Front.* 2023, *7*(7), 1248–1267. DOI: 10.1039/D2QM01220K.

[28] Chourashiya, M. G.; Urakawa, A. Solution Combustion Synthesis of Highly Dispersible and Dispersed Iridium Oxide as an Anode Catalyst in PEM Water Electrolysis. *J Mater Chem A*. 2017, *5*(10), 4774–4778. DOI: 10.1039/C6TA11047A.

[29] Quinson, J. Iridium and IrOx Nanoparticles: An Overview and Review of Syntheses and Applications. *Adv. Colloid Interface Sci.* 2022, *303*, 102643. DOI: 10.1016/j.cis.2022.102643.

[30] Lettenmeier, P.; Wang, L.; Golla-Schindler, U.; Gazdzicki, P.; Cañas, N. A.; Handl, M.; Hiesgen, R.; Hosseiny, S. S.; Gago, A. S.; Friedrich, K. A. Nanosized IrO $_X$ –ir Catalyst with Relevant Activity for Anodes of Proton Exchange Membrane Electrolysis Produced by a Cost-Effective Procedure. *Angew. Chem. Int. Ed.* 2016, *55*(2), 742–746. DOI: 10.1002/anie.201507626.

[31] Lettenmeier, P.; Majchel, J.; Wang, L.; Saveleva, V. A.; Zafeiratos, S.; Savinova, E. R.; Gallet, -J.-J.; Bournel, F.; Gago, A. S.; Friedrich, K. A. Highly Active Nano-Sized Iridium Catalysts: Synthesis and *Operando* Spectroscopy in a Proton Exchange Membrane Electrolyzer. *Chem. Sci.* 2018, *9*(14), 3570–3579. DOI: 10.1039/C8SC00555A.

[32] Glavee, G. N.; Klabunde, K. J.; Sorensen, C. M.; Hadjipanayis, G. C. Borohydride Reduction of Cobalt Ions in Water. Chemistry Leading to Nanoscale Metal, Boride, or Borate Particles. *Langmuir*. 1993, *9*(1), 162–169. DOI: 10.1021/la00025a034.

[33] Glavee, G. N.; Klabunde, K. J.; Sorensen, C. M.; Hadjipanayis, G. C. Borohydride Reduction of Nickel and Copper Ions in Aqueous and Nonaqueous Media. Controllable Chemistry Leading to Nanoscale Metal and Metal Boride Particles. *Langmuir*. 1994, *10*(12), 4726–4730. DOI: 10.1021/la00024a055.

[34] Glavee, G. N.; Klabunde, K. J.; Sorensen, C. M.; Hadjapanayis, G. C. Borohydride Reductions of Metal Ions. A New Understanding of the Chemistry Leading to Nanoscale Particles of Metals, Borides, and Metal Borates. *Langmuir*. 1992, *8*(3), 771–773. DOI: 10.1021/la00039a008.

[35] Shen, J.; Li, Z.; Fan, Y.; Hu, Z.; Chen, Y. Chemically Prepared Fe-B Ultrafine Amorphous Alloy Particles: Influence of the Reaction Time on the Properties. *J. Solid State Chem.* 1993, *106*(2), 493–500. DOI: 10.1006/jssc.1993.1309.

[36] Glavee, G. N.; Klabunde, K. J.; Sorensen, C. M.; Hadjipanayis, G. C. Chemistry of Borohydride Reduction of Iron(II) and Iron(III) Ions in Aqueous and Nonaqueous Media. Formation of Nanoscale Fe, FeB, and Fe2B Powders. *Inorg. Chem.* 1995, *34*(1), 28–35. DOI: 10.1021/ic00105a009.

[37] Kim, S. G.; Brock, J. R. Growth of Ferromagnetic Particles from Cation Reduction by Borohydride Ions. *J. Colloid Interface Sci.* 1987, *116*(2), 431–443. DOI: 10.1016/0021-9797(87)90139-1.

[38] Jackelen, A.-M. L.; Jungbauer, M.; Glavee, G. N. Nanoscale Materials Synthesis. 1. Solvent Effects on Hydridoborate Reduction of Copper Ions. *Langmuir*. 1999, *15*(7), 2322–2326. DOI: 10.1021/la9807311.

[39] Schlesinger, H. I.; Brown, H. C.; Finholt, A. E.; Gilbreath, J. R.; Hoekstra, H. R.; Hyde, E. K. Sodium Borohydride, Its Hydrolysis and Its Use as a Reducing Agent and in the Generation of Hydrogen[1]. *J. Am. Chem. Soc.* 1953, *75*(1), 215–219. DOI: 10.1021/ja01097a057.

[40] Carenco, S.; Portehault, D.; Boissière, C.; Mézailles, N.; Sanchez, C. Nanoscaled Metal Borides and Phosphides: Recent Developments and Perspectives. *Chem. Rev.* 2013, *113*(10), 7981–8065. DOI: 10.1021/cr400020d.

[41] Brown, H. C.; Mead, E. J.; Subba Rao, B. C. A Study of Solvents for Sodium Borohydride and the Effect of Solvent and the Metal Ion on Borohydride Reductions[1]. *J. Am. Chem. Soc.* 1955, *77*(23), 6209–6213. DOI: 10.1021/ja01628a044.

[42] Tsang, C.; Lai, S. Y.; Manthiram, A. Reduction of Aqueous Na_2 WO_4 by $NaBH_4$ at Ambient Temperatures to Obtain Lower Valent Tungsten Oxides. *Inorg. Chem.* 1997, *36*(10), 2206–2210. DOI: 10.1021/ic9610039.

[43] Tsang, C.; Dananjay, A.; Kim, J.; Manthiram, A. Synthesis of Lower Valent Molybdenum Oxides by an Ambient Temperature Reduction of Aqueous K_2 MoO_4 by KBH_4. *Inorg. Chem.* 1996, *35*(2), 504–509. DOI: 10.1021/ic950955w.

[44] Walter, J. C.; Zurawski, A.; Montgomery, D.; Thornburg, M.; Revankar, S. Sodium Borohydride Hydrolysis Kinetics Comparison for Nickel, Cobalt, and Ruthenium Boride Catalysts. *J. Power Sources*. 2008, *179*(1), 335–339. DOI: 10.1016/j.jpowsour.2007.12.006.

[45] Anantharaj, S.; Jayachandran, M.; Kundu, S. Unprotected and Interconnected Ru^0 Nano-Chain Networks: Advantages of Unprotected Surfaces in Catalysis and Electrocatalysis. *Chem. Sci.* 2016, *7*(5), 3188–3205. DOI: 10.1039/C5SC04714E.

[46] Deraedt, C.; Salmon, L.; Gatard, S.; Ciganda, R.; Hernandez, R.; Ruiz, J.; Astruc, D. Sodium Borohydride Stabilizes Very Active Gold Nanoparticle Catalysts. *Chem. Commun.* 2014, *50*(91), 14194–14196. DOI: 10.1039/C4CC05946H.

[47] Demirci, U. B.; Miele, P. Cobalt in NaBH4 Hydrolysis. *Phys. Chem. Chem. Phys.* 2010, *12*(44), 14651. DOI: 10.1039/c0cp00295j.

[48] Li, H.; Zhao, Q.; Wan, Y.; Dai, W.; Qiao, M. Self-assembly of Mesoporous Ni–B Amorphous Alloy Catalysts. *J. Catal.* 2006, *244*(2), 251–254. DOI: 10.1016/j.jcat.2006.08.025.

[49] Tong, D. G.; Wang, D.; Chu, W.; Sun, J. H.; Wu, P. Cobalt–Boron Amorphous Alloy Prepared in Water/Cetyl-Trimethyl-Ammonium Bromide/N-Hexanol Microemulsion as Anode for Alkaline Secondary Batteries. *Electrochim. Acta*. 2010, *55*(7), 2299–2305. DOI: 10.1016/j.electacta.2009.11.082.

[50] Li, H.; Yang, H.; Li, H. Highly Active Mesoporous Co–B Amorphous Alloy Catalyst for Cinnamaldehyde Hydrogenation to Cinnamyl Alcohol. *J. Catal.* 2007, *251*(1), 233–238. DOI: 10.1016/j.jcat.2007.07.022.

[51] Retnamma, R.; Novais, A. Q.; Rangel, C. M. Kinetics of Hydrolysis of Sodium Borohydride for Hydrogen Production in Fuel Cell Applications: A Review. *Int. J. Hydrogen Energy*. 2011, *36*(16), 9772–9790. DOI: 10.1016/j.ijhydene.2011.04.223.

[52] Anantharaj, S.; Jayachandran, M.; Kundu, S. Unprotected and Interconnected Ru ^{0} Nano-Chain Networks: Advantages of Unprotected Surfaces in Catalysis and Electrocatalysis. *Chem. Sci.* 2016, *7*(5), 3188–3205. DOI: 10.1039/C5SC04714E.

[53] Peuckert, M. XPS Study on Thermally and Electrochemically Prepared Oxidic Adlayers on Iridium. *Surf. Sci.* 1984, *144*(2–3), 451–464. DOI: 10.1016/0039-6028(84)90111-0.

[54] Morgan, D. J. Resolving Ruthenium: XPS Studies of Common Ruthenium Materials. *Sur.f Int. Anal.* 2015, *47*(11), 1072–1079. DOI:10.1002/sia.5852.

[55] Hall, H. Y.; Sherwood, P. M. A. X-ray Photoelectron Spectroscopic Studies of the Iridium Electrode System. *J. Chem. Soc. Faraday Trans.* 1984, *80*(1), 135. DOI: 10.1039/f19848000135.

[56] Kim, J.; Shih, P.-C.; Tsao, K.-C.; Pan, Y.-T.; Yin, X.; Sun, C.-J.; Yang, H. High-Performance Pyrochlore-Type Yttrium Ruthenate Electrocatalyst for Oxygen Evolution Reaction in Acidic Media. *J. Am. Chem. Soc.* 2017, *139*(34), 12076–12083. DOI: 10.1021/jacs.7b06808.

[57] Retuerto, M.; Pascual, L.; Calle-Vallejo, F.; Ferrer, P.; Gianolio, D.; Pereira, A. G.; García, Á.; Torrero, J.; Fernández-Díaz, M. T.; Bencok, P., et al. Na-Doped Ruthenium Perovskite Electrocatalysts with Improved Oxygen Evolution Activity and Durability in Acidic Media. *Nat. Commun.* 2019, *10*(1), 2041. DOI: 10.1038/s41467-019-09791-w.

[58] Hubert, M. A.; Gallo, A.; Liu, Y.; Valle, E.; Sanchez, J.; Sokaras, D.; Sinclair, R.; King, L. A.; Jaramillo, T. F. Characterization of a Dynamic $Y_2Ir_2O_7$ Catalyst during the Oxygen Evolution Reaction in Acid. *J Phys Chem C.* 2022, *126*(4), 1751–1760. DOI: 10.1021/acs.jpcc.1c07760.

[59] Mai, L.; Boysen, N.; Subaşı, E.; Arcos, T. D. L.; Rogalla, D.; Grundmeier, G.; Bock, C.; Lu, H.-L.; Devi, A. Water Assisted Atomic Layer Deposition of Yttrium Oxide Using tris(*N,N*′-diisopropyl-2-dimethylamido-guanidinato) Yttrium(iii): Process Development, Film Characterization and Functional Properties. *RSC Adv.* 2018, *8*(9), 4987–4994. DOI: 10.1039/C7RA13417G.

[60] Masuda, Y.; Yamagishi, M.; Koumoto, K. Site-Selective Deposition and Micropatterning of Visible-Light-Emitting Europium-Doped Yttrium Oxide Thin Film on Self-Assembled Monolayers. *Chem. Mater.* 2007, *19*(5), 1002–1008. DOI: 10.1021/cm061303g.